Geochemical Perspectives Letters

Stable strontium isotopes reveal magma-fluid interaction during the evolution of granitic magma

C. Tu, X.-Y. Gao, X.-Q. Chen, O.G. Safonov, M. Ji, X.-F. Gu, X. Hu, Q. Hou, F. Huang

Supplementary Information

The Supplementary Information includes:

- Geological Setting and Samples
- Analytical Methods
- Mineral Sr Contents and Sr Isotopic Compositions
- Details of Geochemical Modelling
- Figures S-1 to S-6
- Tables S-1 to S-13
- Supplementary Information References

Geological Setting and Samples

The Himalayan orogen was built by the continent-continent collision between India and Asia in the Cenozoic (Hodges, 2000; Yin and Harrison, 2000; Yin, 2006). From north to south, this giant orogen is divided into four major lithotectonic units, namely the Tethyan Himalayan Sequence (THS), the Higher Himalayan Crystallines (HHC), the Lower Himalayan Sequence (LHS), and the Sub-Himalaya (SH). These units are separated by the South Tibetan Detachment System (STDS; THS-HHC), Main Central Thrust (MCT; HHC-LHS) and Main Boundary Thrust (MBT; LHS-SH) (Fig. S-1; Yin and Harrison, 2000; Yin, 2006). The Himalayan orogen is also subdivided longitudinally into three regions (Yin, 2006), namely the western Himalaya (west of 81°E), the central Himalaya (81°E–89°E), and the eastern Himalaya (east of 89°E).

Among the major lithotectonic units, the THS is mainly composed of low-grade to unmetamorphosed Phanerozoic sedimentary sequences (Yin, 2006). The HHC mainly consists of Neoproterozoic to Cambrian sediments as well as Neoproterozoic and Early Paleozoic igneous rocks, which have undergone moderate- to high-grade metamorphism in the Cenozoic (Cawood *et al.*, 2007; Richards *et al.*, 2006). Thus, the HHC is generally regarded as the metamorphic

core of the orogen (Hodges, 2000; Kohn, 2014). The LHS is weakly metamorphosed, and the SH is composed of molasse sediments (Yin, 2006). Two giant leucogranite belts are exposed within the Tethyan Himalaya to the north and the Higher Himalaya to the south (Wu *et al.*, 2020). Major pulse of granitic magmatism occurred in the Oligocene to Miocene, with minor activity in the Eocene within the North Himalayan Gneiss Dome of the Tethyan Himalaya (Zeng *et al.*, 2011; Liu *et al.*, 2016). Within the HHC, high-grade metamorphic rocks (e.g., migmatites and granulites) and leucogranites are closely associated. Abundant metamorphic rocks have experienced either fluid-absent or fluid-present melting, leading to the formation of migmatites and granulite. In addition, anatectic rocks such as leucogranites, which are petrogenetically linked to fluid-absent and fluid-present melting of Higher Himalayan metamorphic rocks, have also been identified (Patiño Douce and Harris, 1998; Weinberg, 2016; Gao *et al.*, 2017). The ages of anatexis obtained from most migmatites and granulites are coeval with the formation ages of leucogranites in the Oligocene to Miocene (Kohn, 2014; Weinberg, 2016; Wu *et al.*, 2020).

In this study, we investigated HHC metamorphic rocks and anatectic rocks along the north–south-trending profile of the Cona area in the eastern Himalaya (Fig. S-1). A north–south-trending fault, part of the Sangri–Cona rift, cut across the lithotectonic units of both the THS and HHC. Mainly metapelites and granitic gneisses together with minor calc-silicate rocks and amphibolites outcrop in the area (Xu *et al.*, 2013). Metapelites contain abundant muscovite and biotite while granitic gneisses are predominantly quartzo-feldsparthic rocks. Petrological observations and phase equilibrium modelling show that the metapelites and granitic gneisses have experienced amphibolite to granulite facies metamorphism and partial melting (Ding *et al.*, 2021; Ji *et al.*, 2021). Petrochronological studies of monazites and zircons in supra-solidus metamorphic rocks and leucogranite further constrained that the timing of metamorphism, anatexis and leucogranite magmatism is coeval in the Oligocene to Miocene in this area (Ji *et al.*, 2021, 2022, 2024a). Additionally, whole-rock and monazite Nd isotope analyses for HHC metamorphic rocks (e.g., metasedimentary rocks and granitic gneisses) and leucogranites indicate that the leucogranite magmatism was associated with partial melting of HHC mica schists and granitic gneisses in this area (Ji *et al.*, 2022).

In the field, the anatectic rocks occur primarily as granitic veins and granitic dikes. Granitic veins, typically less than a few centimeters wide, are distributed throughout the migmatitic terrane. They generally occur in parallel layers within migmatitic schists and gneisses and are sometimes ophthalmic due to tectonic deformation (Fig. S-2a, b). Granitic dikes, typically several decimeters thick, are more continuous and can extend for tens of meters parallel to the foliation of surrounding migmatites (Fig. S-2c, d). Due to limitations in rock separation techniques, only granitic dikes and thick veins were studied in detailed in this study. The granite-forming veins and dikes are mainly composed of plagioclase + K-feldspar + quartz, contain various proportions of muscovite and biotite, as well as sporadically bear sillimanite and almandine-rich garnet (Fig. S-3a-f, Table S-1). Melanosomes, representing the residual products of partial melting, are usually found in spatial contact with leucosomes. They are mainly composed of biotite + quartz + plagioclase + K-feldspar. Among the possible protoliths, granitic gneisses are richer in plagioclase and K-feldspar, whereas schists have a greater amount of muscovite and biotite. In total, twenty-one samples of anatectic rocks, seven samples of melanosomes, and eight samples of potential source rocks (5 gneisses and 3 schists) were studied in detail (Fig. S-1; Table S-1).

Analytical Methods

Sample preparation

Sample preparation was conducted at Chengchang Rock and Mineral Testing Technology Service Company, Langfang, China. After removing the altered and weathered surface layers, fresh hand specimens were cut into several small blocks. Some of these blocks were utilized for thin-section production, and others were used for whole-rock powder production and mineral separation. At least 100 g of fresh block was crushed and then powdered in an agate grinder to ensure that the grain sizes of whole-rock powders are above 200 mesh. Rock-forming minerals (e.g., biotite, muscovite, plagioclase, and K-feldspar) grains were roughly picked out from the crushed sample blocks (~80 mesh) using standard magnetic and density separation technologies. The separated mineral grains were then carefully handpicked under a binocular microscope. Whole-rock powders and were utilized for major–trace element, radiogenic Sr–Nd isotope, and stable Sr isotope analyses. Separated minerals were used for trace element, radiogenic Sr isotope, and stable Sr isotope analyses.

Whole-rock major and trace element analyses

Whole-rock major elements were analysed at the State Key Laboratory of Lithospheric and Environmental Coevolution of University of Science and Technology of China, Hefei, China. Trace elements were analysed at ALS Chemex Laboratory in Guangzhou, China and SampleSolution Lab in Wuhan, China. Whole-rock powders were mixed with either lithium borate or lithium metaborate flux and fused in a furnace at ~1000 °C. The resulting flat glass disk was analysed using X-ray fluorescence spectrometry for major elements. Trace element analysis was performed using inductively coupled plasma mass spectrometry (ICP–MS) on solutions after sample powders were dissolved in 4N nitric acid. National standards (granite GSR-1, andesite GSR-2, and basalt GSR-3) and duplicate samples analysed in the same batch suggest that analytical uncertainties are better than ±1–2 % for major elements and better than ±5% for most trace elements. Results of major elements and trace element were list in Table S-5 and Table S-6, respectively.

Whole-rock and mineral stable Sr isotope and radiogenic Sr isotope analyses

Whole-rock and mineral stable Sr isotope and radiogenic Sr isotope analyses were conducted at the State Key Laboratory of Lithospheric and Environmental Coevolution of University of Science and Technology of China, Hefei, China. All the studied samples are fresh. Concentrated HF, HNO_3, and HCl used in the whole chemical procedures were sourced from Fisher Chemical (TraceMetal™ Grade) and purified by double sub-boiling distillation. These reagents were diluted with 18.2 MΩ cm ultra-pure water. All chemical procedures including digestion of whole-rock powders and mineral particles and Sr purification were carried out in an ISO class 6 clean room in USTC, following the protocol established by Chen *et al.* (2022). The Sr recovery rates of these samples were approximately 99 %. The total procedure blank was lower than 100 pg, having a negligible effect relative to the Sr contents (1.5–2.0 μg) in the loaded samples.

Sr isotope compositions were measured using MC-ICP-MS (Neptune Plus, Thermo Fisher Scientific®, Bremen, Germany) in USTC, following the method described by Chen *et al.* (2022). Four Sr isotopes (^{84}Sr, ^{86}Sr, ^{87}Sr and ^{88}Sr) were collected on Faraday cups L2, C, H1, and H2, respectively. In order to correct the isobaric interferences from ^{84}Kr, ^{86}Kr, and ^{87}Rb, Faraday cups L3 and L1 were used to monitor ^{83}Kr and ^{85}Rb. These signals were used to effectively

correct the interferences on ^{84}Sr, ^{86}Sr, and ^{87}Sr. A two-step measurement was applied to obtain $^{87}Sr/^{86}Sr$ and $\delta^{88/86}Sr$ values. Firstly, $^{86}Sr/^{88}Sr = 0.1194$ (Nier, 1938) and the exponential law was used to correct instrument mass bias for $^{87}Sr/^{86}Sr$ in an unspiked measurement. Secondly, an ^{84}Sr-^{87}Sr double-spike (^{84}Sr = 52.1 %, ^{86}Sr = 2.7 %, ^{87}Sr = 32.4 %, ^{88}Sr = 12.8 %) was added into the sample solution ($Sr_{DS}/Sr_{sample} \sim 0.7$) for mass bias calibration. The standard-sample-bracketing (SSB) method are used to correct the instrumental isotopic fractionation in $\delta^{88/86}Sr$ analysis. The stable Sr isotopic composition is expressed in per mil (‰) is as follows:

$$\delta^{88/86}Sr = \left[\left(^{88}Sr/^{86}Sr\right)_{Sample}/\left(^{88}Sr/^{86}Sr\right)_{SRM\ 987}\right] - 1 \quad \text{(S-1)}$$

where SRM 987 from the National Institute of Standards and Technology of the United States of America was used as the bracketing standard during the measurements. Our $\delta^{88/86}Sr$ results for the USGS reference materials (Table S-2) are +0.33 ± 0.03 ‰ (2SD, n = 8) for G-2, +0.25 ± 0.01 ‰ (2SD, n = 8) for AGV-2, +0.26 ± 0.02 ‰ (2SD, n = 4) for BHVO-2 and +0.19 ± 0.00 ‰ (2SD, n = 4) for RGM-1, which are consistent with the literature data (Chen *et al.*, 2022 and references therein). The $\delta^{88/86}Sr$ and $^{87}Sr/^{86}Sr$ results for samples are list in Table S-3.

Whole-rock radiogenic Nd isotope analyses

Whole-rock Nd isotope analyses, including chemical separation and measurement procedures, were conducted at the State Key Laboratory of Lithospheric and Environmental Coevolution of University of Science and Technology of China (USTC), Hefei, China. Whole-rock powders (tens of milligrams) were dissolved in clean Teflon bombs with purified HF + $HClO_4$, and then, chemical separations of Nd were performed using conventional ion exchange procedures. Whole-rock Sm–Nd isotope measurements were performed on a Neptune Plus multicollector inductively coupled plasma mass spectrometry (MC-ICP-MS). Total analytical blanks are <50 pg for Nd. During data acquisition, the measured $^{143}Nd/^{144}Nd$ ratio for the JNdi-1 Nd standard was 0.512099 ± 4 (2SD, n = 5). Reference materials AGV-2, RGM-2 and GSP-2 were measured to monitor the accuracy and precision of the whole analytical procedures, yielding $^{143}Nd/^{144}Nd$ ratios of 0.512784± 6 (2SE, n = 1), 0.512791 ± 6 (2SE, n = 1) and 0.511375 ± 6 (2SE, n = 1), respectively. These values are consistent with the recommended values within analytical error (GeoREM, http://georem.mpch-mainz.gwdg.de/). To calculate the initial Nd isotope compositions of the samples, parent/daughter ratios (Sm/Nd) were derived from the measured whole-rock trace element compositions, which were list in Table S-4.

Mineral Sr Contents and Sr Isotopic Compositions

Determining Sr contents and Sr isotopic compositions for Sr-bearing rock-forming minerals are prerequisite for investigating the Sr isotope behaviour during processes of partial melting and fractional crystallisation. In this study, precise and comprehensive analyses reveal significant differences in Sr contents and Sr isotopic compositions among plagioclase (Pl), K-feldspar (Kfs), muscovite (Ms), and biotite (Bt) in all lithology (Fig. S-5; Table S-3). The Sr contents in these minerals are 185~354 μg/g in plagioclase, 79~150 μg/g in K-feldspar, 7~23 μg/g in muscovite and ~1.5 μg/g in

biotite. Therefore, the Sr contents follow the order Pl > Kfs >> Ms > Bt (Fig. S-5a), which is consistent with the known partitioning behaviour of Sr in minerals. Therefore, whole-rock Sr contents is mainly controlled by feldspar. In contrast, the radiogenic Sr isotopic compositions follow the order Bt > Ms > Kfs > Pl (Fig. S-5a), which may be related to high Rb/Sr ratios in mica. However, distinct patterns are observed in stable Sr isotopic compositions (Fig. S-5b). $\delta^{88/86}$Sr values for muscovite (+0.083 ~ +0.467 ‰) and plagioclase (+0.077 ~ +0.402 ‰) are higher than those for biotite (0.313 ‰) and K-feldspar (-0.066 ~ +0.233 ‰) (Table S-1). The $\delta^{88/86}$Sr values of plagioclase and muscovite separates tend to be heavier than their whole rocks ($\Delta^{88/86}Sr_{Pl\text{-}Bulk}$ = -0.02 to +0.02 ‰ and $\Delta^{88/86}Sr_{Ms\text{-}Bulk}$ = -0.04 to +0.21 ‰). The $\delta^{88/86}$Sr values of K-feldspar and biotite separates tend to be lighter than their whole rocks ($\Delta^{88/86}Sr_{Kfs\text{-}Bulk}$ = -0.13 to -0.04 ‰ and $\Delta^{88/86}Sr_{Bt\text{-}Bulk}$ = -0.07 ‰). Overall, the mineral $\delta^{88/86}$Sr values decrease in the order of Pl > Ms > Bt > Kfs.

In the absence of relevant experiments and first-principles calculations, the fractionation coefficients of stable Sr isotope between minerals and melt are estimated based on the measured values of Sr-bearing minerals in this study (Fig. S-5b; Table S-1). Isotopic fractionation is strongly influenced by ionic environment, coordination number, bond length, and bond strength, where heavier isotopes preferentially enter phases with stronger chemical bonds (Urey, 1947; Schauble, 2004). Sr typically occurs in a bivalent state (Sr^{2+}). In plagioclase, Sr^{2+} mainly substitutes for Ca^{2+} in an VIII-fold coordinated site, with Sr-O bond lengths ranging from 2.59 to 2.69 Å (Shannon, 1976; Blundy and Wood, 1994; Wood and Blundy, 1997; Sun *et al.*, 2017). In K-feldspar, Sr^{2+} can substitute for the larger K^+ ion in a similar coordination environment (VIII-fold coordinated site), but the Sr-O bond lengths are longer (2.84 to 2.85 Å; Shannon, 1976; Arzilli *et al.*, 2018). This suggest that lighter stable Sr isotopes preferentially enter K-feldspar (Chen *et al.*, 2025). Based on theoretical speculation and actual observations, the estimated stable Sr isotope fractionation values between minerals and melts in the following modelling were taken as following: $\Delta^{88/86}Sr_{Pl\text{-}melt}$ = +0.02 ‰; $\Delta^{88/86}Sr_{Kfs\text{-}melt}$ = -0.13 ‰; $\Delta^{88/86}Sr_{Ms\text{-}melt}$ = +0.21 ‰; $\Delta^{88/86}Sr_{Bt\text{-}melt}$ = -0.07 ‰.

Details of Geochemical Modelling

Geochemical modelling of stable Sr isotopic fractionation during partial melting

During partial melting, both mineral assemblages and modal proportions of melt (X_{melt}) and residual minerals ($X_{mineral\ \alpha}$) vary with temperature and pressure that may result in stable Sr isotope fractionation between melt and residual rock. In this study, we conducted phase equilibrium modelling using Perple_X 7.1.6 software (Connolly, 2005) to determine the evolution of mineral assemblages and modal proportion of melt and residual minerals (X_{melt} and $X_{mineral\ \alpha}$) during partial melting of two potential source rocks, mica schists and granitic gneisses.

Phase equilibrium modelling was performed in the MnO-Na_2O-CaO-K_2O-FeO-MgO-Al_2O_3-SiO_2-H_2O-TiO_2-O (MnNCKFMASHTO) system, with an internally consistent thermodynamic database of hp11ver.dat (Holland and Powell, 2011). Solution models for granitic melt, garnet, muscovite, biotite, staurolite, orthopyroxene, cordierite (White *et al.*, 2014), plagioclase and K-feldspar (Fuhrman and Lindsley, 1988), clinopyroxene (Holland and Powell, 1996), spinel (White *et al.*, 2002), and ilmenite (White *et al.*, 2000) were used. Kyanite, sillimanite, rutile, quartz, and H_2O were considered pure phases. The average compositions of metapelite and granitic gneiss of the Himalayan orogen (Ji *et al.*, 2022) were used in the modelling. Considering that the peak metamorphic conditions for crustal rocks in the

Himalayan orogen span a pressure and temperature range of ~0.6–1.8 GPa and ~700–970 °C (Ji *et al.*, 2024a, 2024b), partial melting via isobaric heating at 1.5, 1.0, and 0.5 GPa over a temperature range of 700 to 900°C was considered here.

The representative average Sr contents of mica schist (C^{Sr}_{Source} = 77.8 μg/g) and granitic gneiss (C^{Sr}_{Source} = 70.4 μg/g) from the Cona area in eastern Himalaya (Ji *et al.*, 2022, 2023) were used in the modelling. The calculated average stable Sr isotopic compositions ($\delta^{88/86}Sr_{source}$)are 0.288 ‰ and 0.216 ‰ for mica schist and granitic gneiss, respectively. Then, the Sr contents of melt (C^{Sr}_{melt}) can be calculated using the equation for batch melting (Shaw, 1970; Hanson, 1978):

$$C^{Sr}_{melt} = C^{Sr}_{source}/[D^{Sr}\times(1-F)+F] \quad \text{(S-2)}$$

where F is the weight fraction of melt in the rock system, and D^{Sr} is the bulk partition coefficient between residue and melt, which can be calculated by the following equation:

$$D^{Sr} = \Sigma^{n}_{\alpha=1}\left(D^{Sr}_{mineral\ \alpha/melt} \times X_{mineral\ \alpha}\right) \quad \text{(S-3)}$$

where $X_{mineral\ \alpha}$ is the weight fraction of each mineral in residue, and ($D^{Sr}_{mineral\ \alpha/melt}$) is mineral/melt partition coefficients for Sr, which were obtained from the literatures: Kfs and Bt (Nash and Crecraft, 1985), Pl (Bacon and Druitt, 1988), Ms (Icenhower and London, 1995). $D^{Sr}_{plagioclase/melt}$ = 4.47; $D^{Sr}_{K\text{-}feldspar/melt}$ = 3.87; $D^{Sr}_{biotite/melt}$ = 0.22; $D^{Sr}_{muscovite/melt}$ = 0.05. The Sr contents of residue ($C^{Sr}_{residue}$) were calculated using the mass balance equation:

$$C^{Sr}_{source} = F \times C^{Sr}_{melt} + (1 - F) \times C^{Sr}_{residue} \quad \text{(S-4)}$$

Assuming melt-residue equilibrium throughout the melting process, the stable Sr isotopic compositions of melt ($\delta^{88/86}Sr_{melt}$) and residue ($\delta^{88/86}Sr_{residue}$) were estimated using the isotope mass balance equations:

$$\delta^{88/86}Sr_{source} = f^{Sr}_{melt} \times \delta^{88/86}Sr_{melt} + (1\text{-}f^{Sr}_{melt}) \times \delta^{88/86}Sr_{residue} \quad \text{(S-5)}$$

$$\delta^{88/86}Sr_{residue} = \delta^{88/86}Sr_{melt} + \Delta^{88/86}Sr_{residue\text{-}melt} \quad \text{(S-6)}$$

where f^{Sr}_{melt} is the mass fraction of Sr entering melt, which equals $\frac{F\times C^{Sr}_{melt}}{C^{Sr}_{source}}$, and $\Delta^{88/86}Sr_{residue\text{-}melt}$ is bulk fractionation factors of stable Sr isotope between residue and melt, which were calculated as follows:

$$\Delta^{88/86}Sr_{residue\text{-}melt} = \frac{\sum^{n}_{\alpha=1}(D^{Sr}_{mineral\ \alpha/melt} \times X_{mineral\ \alpha} \times \Delta^{88/86}Sr_{mineral\ \alpha\text{-}melt})}{\sum^{n}_{\alpha=1}(D^{Sr}_{mineral\ \alpha/melt} \times X_{mineral\ \alpha/melt})} \quad \text{(S-7)}$$

where $\Delta^{88/86}Sr_{mineral\ \alpha\text{-}melt}$ is the individual mineral-melt Sr isotope fractionation factor. The values used here are based on empirical estimates derived from our measurements of Sr-bearing minerals (see previous section). The results of phase equilibrium modelling are listed in Table S-7 and Table S-8, and the calculated $\delta^{88/86}Sr$ values under different temperature and pressure are shown in Figures 2a-c and S-6 and Table S-9.

Geochemical modelling of radiogenic Sr isotopic fractionation during partial melting

To model the radiogenic Sr isotope composition of melt, we assumed constant Sr contents ($C_{mineral\ \alpha}$) and $^{87}Sr/^{86}Sr$ ratios ($(^{87}Sr/^{86}Sr)_{i\ mineral\ \alpha}$) for each mineral during melting processes. In this study, the relatively homogeneous radiogenic Sr isotopic composition of the protoliths and the broadly similar Sr contents and $(^{87}Sr/^{86}Sr)_i$ values of the same mineral species across different rock types. Therefore, we selected individual minerals from sample 19T93 and biotite from sample 19T109B as representation for our calculations, where C^{Sr}_{Pl} = 353.9 μg/g and $(^{87}Sr/^{86}Sr)_i$ = 0.746872 in Pl; C^{Sr}_{Ms} = 23.2 μg/g and $(^{87}Sr/^{86}Sr)_i$ = 0.750875 in Ms; C^{Sr}_{Kfs} = 110.4 μg/g and $(^{87}Sr/^{86}Sr)_i$ = 0.747085 in Kfs; C^{Sr}_{Bt} = 1.3 μg/g and $(^{87}Sr/^{86}Sr)_i$ = 0.841032 in Bt. An additional assumption that must be stated is that the influence of Rb radioactive decay on the radiogenic Sr isotopes of the Miocene anatectic rocks in the Cona area can be considered negligible due to their young geological age. Then, the $(^{87}Sr/^{86}Sr)_i$ ratios of melts were calculated following the equation from Knesel and Davidson (2002):

$$(^{87}Sr/^{86}Sr)_{i\ melt} = \frac{\sum (X_{mineral\ \alpha} \times D^{Sr}_{mineral\ \alpha} \times C^{Sr}_{mineral\ \alpha} \times (^{87}Sr/^{86}Sr)_{i\ mineral\ \alpha})}{\sum (X_{mineral\ \alpha} \times D^{Sr}_{mineral\ \alpha} \times C_{mineral\ \alpha})} \quad \text{(S-8)}$$

where $X_{mineral\ \alpha}$ is the modal proportion of mineral α that was consumed during partial melting, which can by obtain by mineral proportion difference between sub-solidus and super-solidus. Modelled mineral assemblages and modal proportions of minerals and melt during partial melting of mica schist and gneiss across different anatectic temperature and pressure are listed in Supplementary Table S-7. The calculation results are shown in Supplementary Table S-9. Although elevated temperature, low pressure, and high water activity can lead to higher Sr isotopic ratios, the simulated melt Sr isotopic compositions remain only marginally different from those of the protolith. This minor fractionation is insufficient to account for the highly radiogenic Sr isotopic signatures, i.e. $(^{87}Sr/^{86}Sr)_i > 1$, observed in the studied anatectic rocks. Therefore, the anomalously high radiogenic Sr isotopic ratios in the Cona anatectic rocks cannot be attributed to partial melting.

Geochemical modelling of stable Sr isotopic fractionation during fractional crystallisation

During fractional crystallisation, mineral assemblages and modal proportions of melt and crystallised minerals would also vary with temperature and pressure, which may result in stable Sr isotope fractionation between melt and residual solid rock. We performed phase equilibrium modelling for fractional crystallisation using the Perple_X 7.1.6 software (Connolly, 2005). The modelling was performed in the MnO-Na_2O-CaO-K_2O-FeO-MgO-Al_2O_3-SiO_2-H_2O-TiO_2-O

(MnNCKFMASHTO) system, with an internally consistent thermodynamic dataset of hp11ver.dat (Holland and Powell, 2011). Solution models for granitic melt, garnet, muscovite, biotite, staurolite, orthopyroxene, cordierite (White *et al.*, 2014), plagioclase and K-feldspar (Fuhrman and Lindsley, 1988), spinel (White *et al.*, 2002), and ilmenite (White *et al.*, 2000) were used in the modelling. Kyanite, sillimanite, rutile, quartz, and H_2O were considered pure phases. The major and trace element compositions of two representative anatectic rocks（19T109A and 22XZ153L) were utilized in the modelling. Their water content (6 wt.%) and $Fe^{3+}/(Fe^{2+} + Fe^{3+})$ ratio (0.17) were referred to those of parental leucogranite magmas (Scaillet *et al.*, 1995). The modelling was performed from supra-solidus (950°C) to the solidus under the pressure of 5 kbar, which are similar to the crystallisation experiment of leucogranite magma (Scaillet *et al.*, 1995).

The modelled results are listed in Table S-10. The effects of fractional crystallisation on Sr contents in residual melts (C^{Sr}_{melt}) was evaluated using the Rayleigh fractionation equations:

$$C^{Sr}_{melt} = C^{Sr}_{initial} \cdot (1 - F)^{(D^{crystal/melt}_{Sr} - 1)} \quad \text{(S-9)}$$

where C^{Sr}_{melt} is the Sr contents in the differentiated melt, $C^{Sr}_{initial}$ is the initial melt Sr composition, and F is the degree of crystallisation. $D^{crystal/melt}_{Sr}$ is the bulk partitioning coefficient for Sr between crystallised minerals and melt, which was calculated as:

$$D^{crystal/melt}_{Sr} = \Sigma^{n}_{\alpha=1}\left(D^{mineral\ \alpha/melt}_{Sr} \times X_{mineral\ \alpha}\right) \quad \text{(S-10)}$$

where $X_{mineral\ \alpha}$ is weight fraction of mineral in crystallising assemblage, $D^{mineral\ \alpha/melt}_{Sr}$ is the mineral/melt partitioning coefficient for Sr, with values sourced from literature (Kfs and Bt: Nash and Crecraft, 1985; Pl: Bacon and Druitt, 1988; Ms: Icenhower and London, 1995).

The $\delta^{88/86}Sr$ values of the residual melts ($\delta^{88/86}Sr_{melt}$) were then calculated using:

$$\delta^{88/86}Sr_{melt} = \delta^{88/86}Sr^{0}_{melt} + \Delta^{88/86}Sr_{crystal\text{-}melt} \cdot \ln(f^{Sr}_{melt}) \quad \text{(S-11)}$$

$$f^{Sr}_{melt} = \frac{(1 - F) \cdot C^{Sr}_{melt}}{C^{0}_{melt}} \quad \text{(S-12)}$$

where $\delta^{88/86}Sr^{0}_{melt}$ is the initial stable Sr isotopic composition of melt, f^{Sr}_{melt} is the remaining fraction of Sr in the melt, and $\Delta^{88/86}Sr_{crystal\text{-}melt}$ is the Sr isotope fractionation factors between crystallised minerals and melt, which were calculated by:

$$\Delta^{88/86}Sr_{crystal\text{-}melt} = \frac{\sum_{\alpha=1}^{n}(D_{Sr}^{mineral\ \alpha/melt} \times X_{mineral\ \alpha} \times \Delta^{88/86}Sr_{mineral\ \alpha})}{\sum_{\alpha=1}^{n}(D_{Sr}^{minral\ \alpha} \times X_{mineral\ \alpha})} \quad (S\text{-}13)$$

where $\Delta^{88/86}Sr_{mineral\ \alpha\text{-}melt}$ is mineral-melt Sr isotope fractionation factor, whose values have been described in the previous sections. The calculated results are plotted in Figure 2d and list in Table S-11.

Geochemical modelling of stable Sr isotopic fractionation during magma-fluid interaction

Feldspar-dominated crystallisation would lead to a sharp decline in Sr content of the residual melts. Based on fractional crystallisation modelling, several end-members compositions were selected to represent different degrees of differentiation. On this basis, we performed a geochemical modelling of magma-fluid interaction to investigate the behavior of stable Sr isotope during this process. The Sr contents and $\delta^{88/86}Sr$ values of the mixtures between magma and fluid (C_{mix}^{Sr} and $\delta^{88/86}Sr_{mix}$) were calculated using the mass balance equations:

$$C_{mix}^{Sr} = f_{fluid} \cdot C_{fluid}^{Sr} + (1 - f_{fluid}) \cdot C_{melt}^{Sr} \quad (S\text{-}14)$$

$$\delta^{88/86}Sr_{mix} \cdot C_{mix}^{Sr} = \delta^{88/86}Sr_{fluid} \cdot f_{fluid} \cdot C_{fluid}^{Sr} + \delta^{88/86}Sr_{melt} \cdot (1 - f_{fluid}) \cdot C_{melt}^{Sr} \quad (S\text{-}15)$$

where f_{fluid} is the weight fraction of the fluid component in the mixtures. The results are shown in Figure 2d and Table S-12.

Supplementary Figures

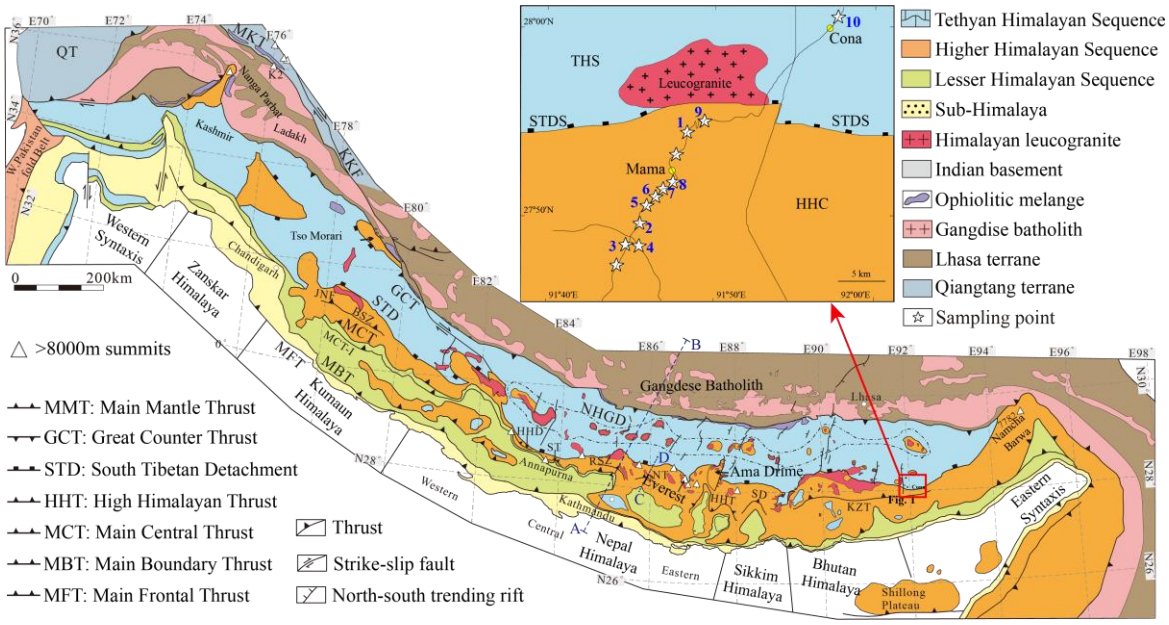

Figure S-1 Schematic geological map of the Himalayan orogen (modified after Yin, 2006; Wang *et al.*, 2022) and the Cona area in the eastern Himalaya (modified after Ji *et al.*, 2021). The locations of the studied anatectic rocks, migmatites, and potential source rocks are labeled with the asterisks and their GPS is described in detail in the Supplementary Table S-1. SH—Sub-Himalaya; LHS—Lower Himalayan Sequence; QT—Qiangtang Terrane; MKT—Main Karakorum Thrust; KKF—Karakorum Thrust; JNF—Jhala Normal Fault; BSZ—Badrinath Shear Zone; ST Sinuwa Thrust; RSZ Rasuwagadhi Shear Zone; NT Nyalam Thrust; NHGD North Himalayan Gneiss Dome; KZT Kakhtang-Zimithang Thrust.

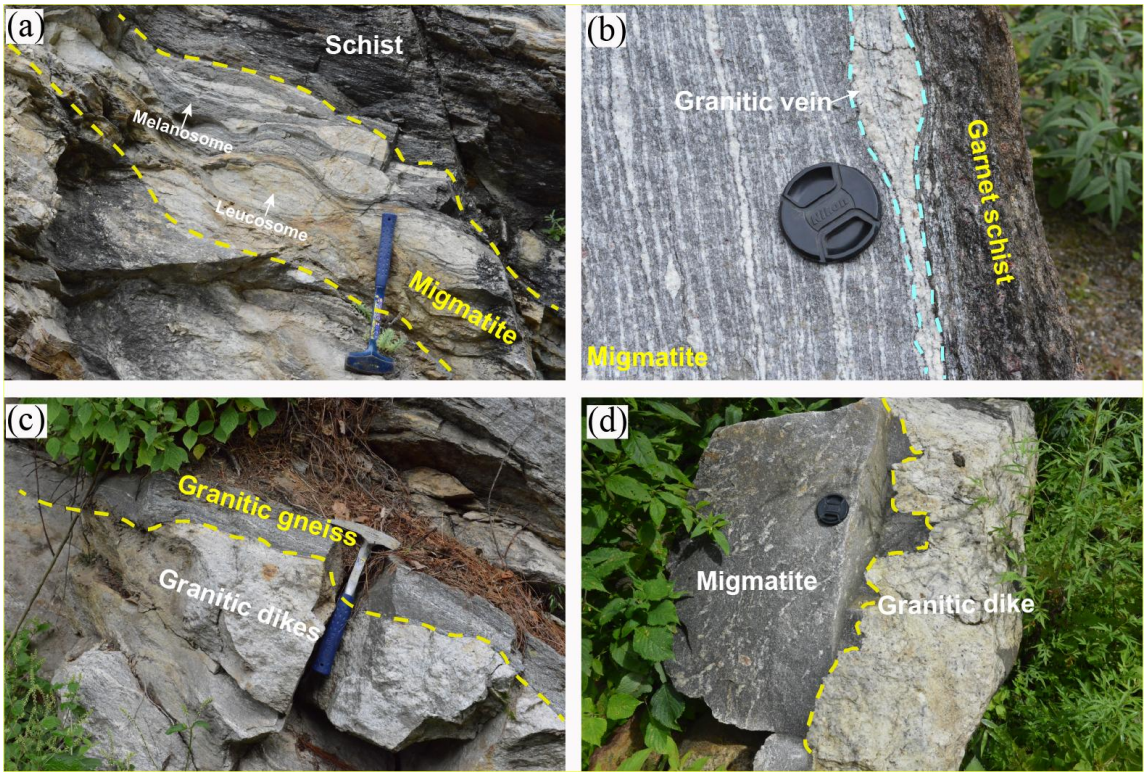

Figure S-2 Field photographs of the schist, gneiss, and migmatite from the Cona area in the eastern Himalaya. **(a)** Ophthalmic leucosomes and bedded melanosomes are surrounded by schists. **(b)** Stromatic migmatites are composed of melanosome and leucosome, which are in contact with granitic vein and garnet schist. **(c) (d)** Granitic dike with several decimetres thick intruding into gneiss.

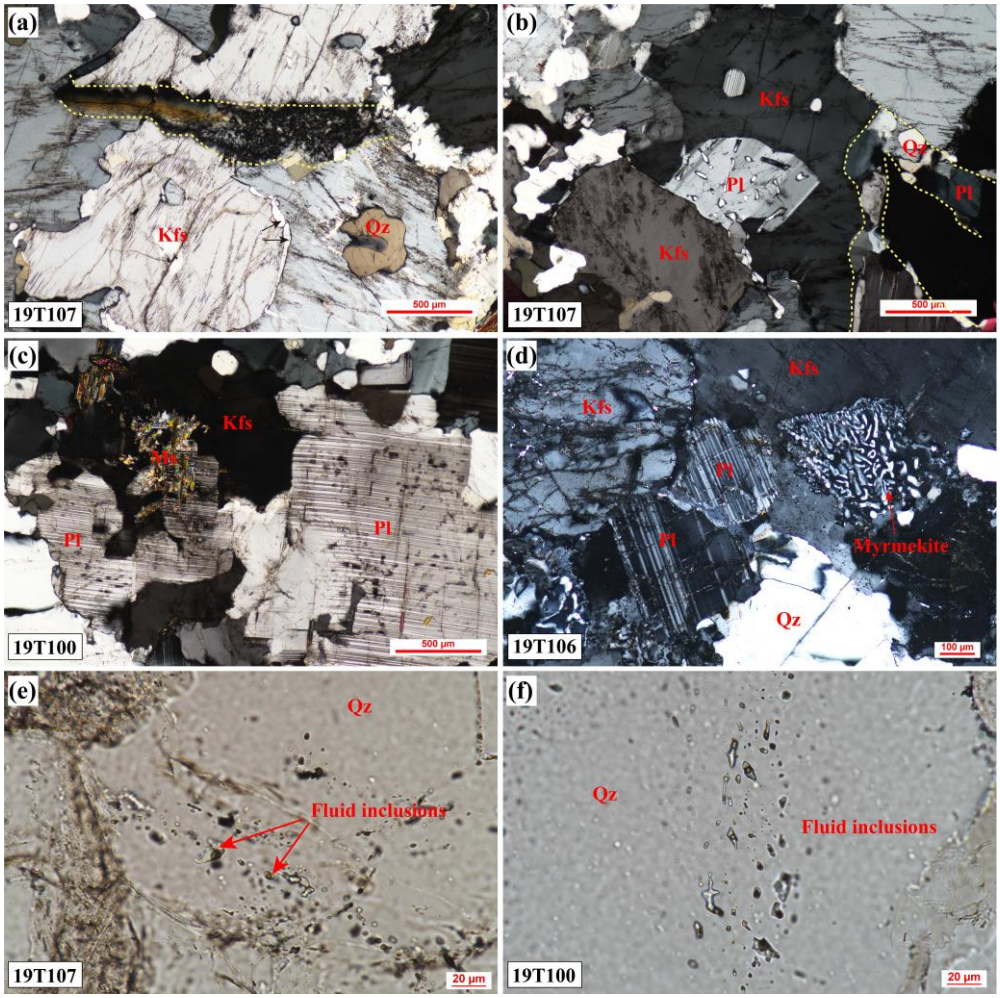

Figure S-3 Photomicrographs of three leucosome samples with extremely low $\delta^{88/86}$Sr values from the Cona area in the eastern Himalaya. **(a)** K-feldspar grain margins are surrounded by plagioclase and quartz, forming quartz films (black arrows) and quartz-feldspar aggregates (yellow line area) in grain boundaries. **(b)** Plagioclase and quartz assembly replaces the intergranular K-feldspar. **(c)** Embayed margins of plagioclase are replaced by muscovite and K-feldspar. Metasomatic structure in the same direction inside K-feldspar. **(d)** Subhedral plagioclase and myrmekite are encapsulated by the giant metasomatic K-feldspar. **(e) (f)** Densely packed clusters of fluid inclusions in quartz. Mineral abbreviations are from Whitney and Evans (2010).

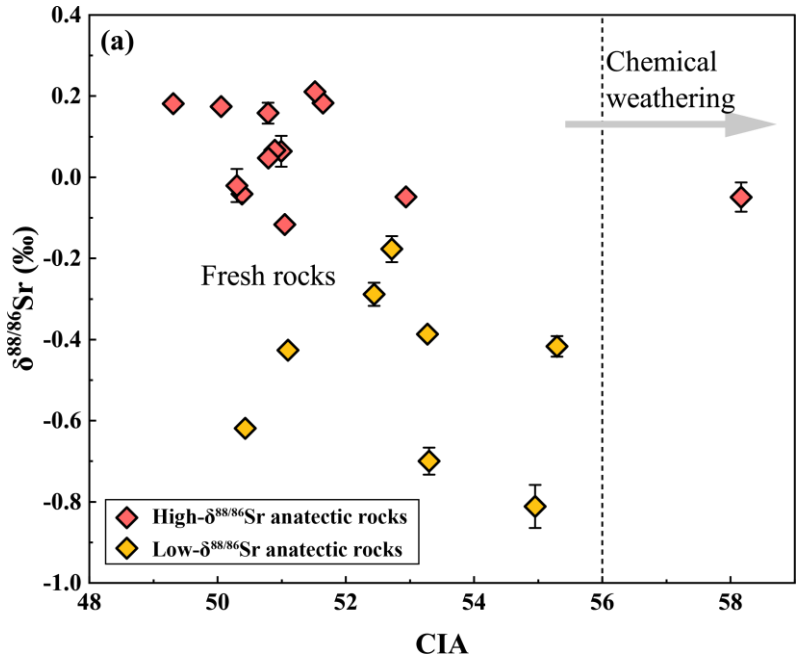

Figure S-4 Plots of $\delta^{88/86}Sr$ values and chemical index of alteration (CIA) for anatectic rocks from the Cona area in eastern Himalaya. The gray arrow indicates the increasing of CIA with the stronger chemical weathering. CIA = mol. Al_2O_3 / (Al_2O_3 + CaO + Na_2O + K_2O) (Nesbitt and Young, 1982).

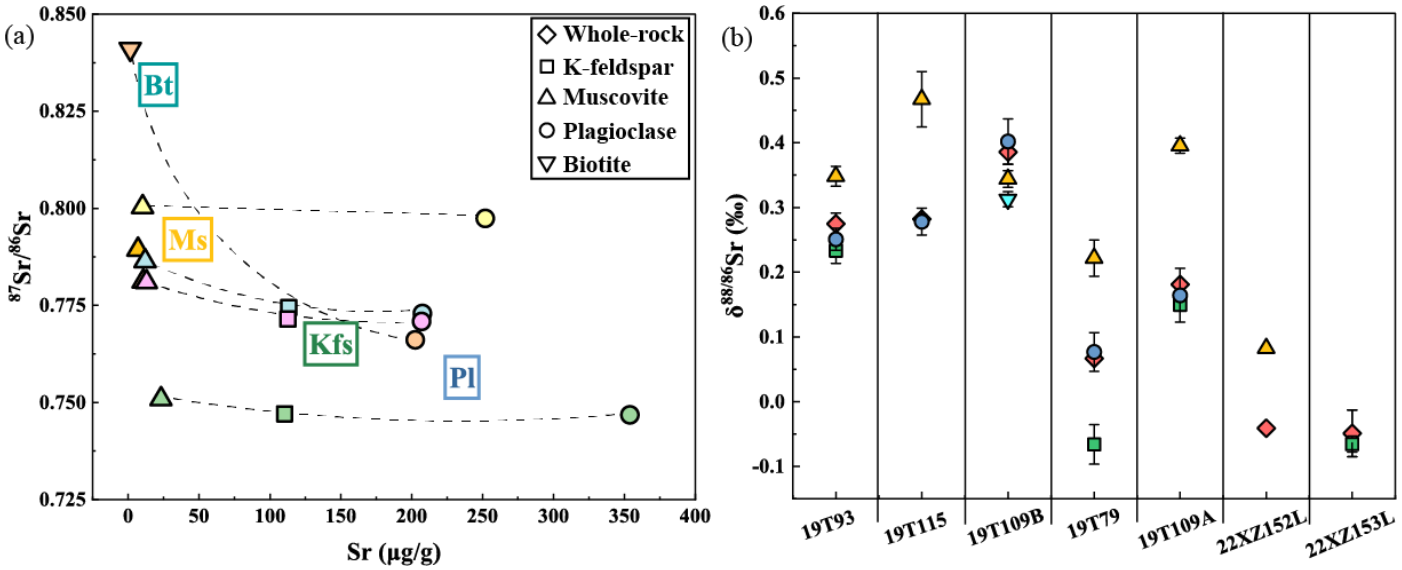

Figure S-5 **(a)** Plot of measured $^{87}Sr/^{86}Sr$ ratios and Sr contents for Sr-bearing rock-forming minerals in rocks from the Cona area in the eastern Himalaya. Different shapes of the symbols represent different minerals. Symbols with the same colour represent the same sample, which are connected by a dotted line. **(b)** A comparison of $\delta^{88/86}Sr$ values for whole-rock and Sr-bearing rock-forming minerals in rocks from the Cona area in the eastern Himalaya. Source rocks are 19T93 (granitic gneiss) and 19T115 (mica schist). Melanosome is 19T109B and rocks include four samples (19T79, 19T109A, 22XZ152L, 22XZ153L).

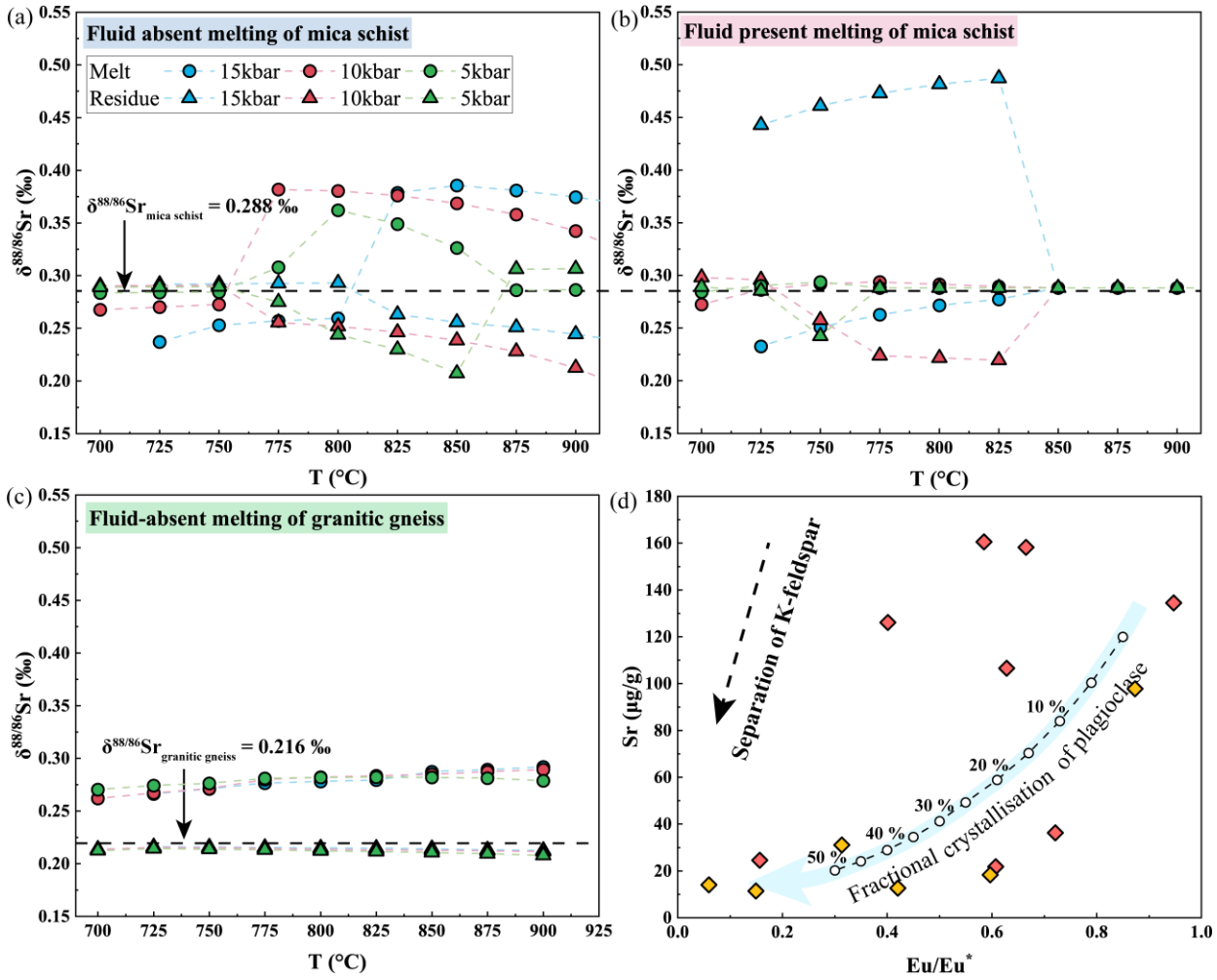

Figure S-6 (a–c) Stable Sr isotopic fractionation between melt and solid rock as a function of anatectic temperature and pressure using phase equilibrium modelling. In addition, the modelling investigated the influence of source rock type (a. mica schist and c. granitic gneiss) and water contents (a. lower water content and b. higher water content). **(d)** Plot of Eu/Eu* and Sr contents for anatectic rocks from the Cona area in eastern Himalaya. The dash line in blue arrow is Rayleigh model for separation of plagioclase and the black arrow represent the direction of separation of K-feldspar. See section **Modelling of partial melting** in Supplementary Information for modal details.

Supplementary Tables

Table S-1 Locations and mineral assemblages of studied rocks from the Cona area, southern Tibet, in the eastern Himalaya.

Table S-2 Stable Sr isotopic and radiogenic Sr isotopic compositions for USGS reference materials.

Table S-3 Whole-rock and mineral stable Sr isotopic and radiogenic Sr isotopic compositions for anatectic rocks, migmatites, and potential source rocks from the Cona area in eastern Himalaya.

Table S-4 Whole-rock Nd isotopic compositions for anatectic rocks, migmatites, and potential source rocks from the Cona area in eastern Himalaya.

Table S-5 Whole-rock major element compositions for anatectic rocks, migmatites, and potential source rocks from the Cona area in eastern Himalaya.

Table S-6 **(a)** Whole-rock and mineral trace element compositions for anatectic rocks, migmatites, and potential source rocks from the Cona area in eastern Himalaya. **(b)** Sr (μg/g) contents in minerals determined by LA-ICP-MS.

Table S-7 Modelled mineral assemblages and modal proportions of minerals and melt during partial melting of mica schist and granitic gneiss across different anatectic temperature and pressure.

Table S-8 Modelled major and trace compositions of melt during partial melting of mica schist and gneiss across different anatectic temperature and pressure.

Table S-9 Modelled Sr contents and, stable Sr and radiogenic Sr isotopic compositions of melt and residue during partial melting.

Table S-10 Modelled mineral assemblages and modal proportions of minerals and melts during fraction crystallisation of two representative anatectic rocks across different temperatures at 5 kbar.

Table S-11 Modelled Sr contents and stable Sr isotopic compositions of differentiated melts during fractional crystallisation.

Table S-12 Modelled Sr contents and stable Sr isotopic compositions of mixture of melts and fluids during magma-fluid interaction.

Table S-13 Parameters used in modelling stable Sr isotopic fractionation during crystal fractionation and partial melting in the anatectic rocks from the Cona area in eastern Himalaya.

Tables S-1 to S-13 are available for download (.xlsx) from the online version of this article at https://doi.org/10.7185/geochemlet.2535.

Supplementary Information References

Arzilli, F., Fabbrizio, A., Schmidt, M.W., Petrelli, M., Maimaiti, M., Dingwell, D.B., Paris, E., Burton, M., Carroll, M.R. (2018) The effect of diffusive re-equilibration time on trace element partitioning between alkali feldspar and trachytic melts. *Chemical Geology* 495, 50–66. https://doi.org/10.1016/j.chemgeo.2018.07.035

Bacon, C.R., Druitt, T.H. (1988) Compositional evolution of the zoned calcalkaline magma chamber of Mount Mazama, Crater Lake, Oregon. *Contributions to Mineralogy and Petrology* 98, 224–256. https://10.1007/BF00402114

Blundy, J., Wood, B. (1994) Prediction of crystal-melt partition-coefficients from elastic-moduli. *Nature* 372, 452–454. https://doi.org/10.1038/372452a0

Cawood, P.A., Johnson, M.R.W., Nemchin, A.A. (2007) Early Palaeozoic orogenesis along the Indian margin of Gondwana: Tectonic response to Gondwana assembly. *Earth and Planetary Science Letters* 255, 70–84. https://doi.org/10.1016/j.epsl.2006.12.006

Chen, X.-Q., Zeng, Z., Yu, H.-M., Sun, N., Huang, F. (2022) Precise measurements of $\delta^{88/86}$Sr for twenty geological reference materials by double-spike MC-ICP-MS. *International Journal of Mass Spectrometry* 479, 116883. https://doi.org/10.1016/j.ijms.2022.116883

Chen, X., Deng, G., Jiang, D., Nan, X., Huang, F. (2025) Stable strontium isotope fractionation during crystal-melt separation in granitic magma evolution. *Acta Geochimica* 44, 731–739. https://doi.org/10.1007/s11631-024-00752-9

Connolly, J.A.D. (2005) Computation of phase equilibria by linear programming: a tool for geodynamic modeling and its application to subduction zone decarbonation. *Earth and Planetary Science Letters* 236, 524–541. https://doi.org/10.1016/j.epsl.2005.04.033

Dai, F.-Q., Zhao, Z.-F., Zheng, Y.-F. (2017) Partial melting of the orogenic lower crust: Geochemical insights from post-collisional alkaline volcanics in the Dabie orogen. *Chemical Geology* 454, 25–43. https://doi.org/10.1016/j.chemgeo.2017.02.022

Ding, H.X., Kohn, M.J., Zhang, Z.-M. (2021) Long-lived (ca. 22-24 Myr) partial melts in the eastern Himalaya: Petrochronologic constraints and tectonic implications. *Earth and Planetary Science Letters* 558, 116764. https://doi.org/10.1016/j.epsl.2021.116764

Fuhrman, M.L., Lindsley, D.H. (1988) Ternary-feldspar modeling and thermometry. *American Mineralogist* 73, 201–215.

Gao, L.-E., Zeng, L.-S., Asimow, P.D. (2017) Contrasting geochemical signatures of fluid-absent versus fluid-fluxed melting of muscovite in metasedimentary sources: The Himalayan leucogranites. *Geology* 45, 39–42. https://doi.org/10.1130/G38336.1

Hanson, G.N. (1978) The application of trace elements to the petrogenesis of igneous rocks of granitic composition. *Earth and Planetary Science Letters* 38, 26–43. https://doi.org/10.1016/0012-821X(78)90124-3

Hodges, K.V. (2000) Tectonics of the Himalaya and southern Tibet from two perspectives. *Bulletin of the Geological Society of America* 112, 324–350. https://doi.org/10.1130/0016-7606(2000)112<324:TOTHAS>2.0.CO;2

Holland, T., Powell, R. (1996) Thermodynamics of order-disorder in minerals: II. Symmetric formalism applied to solid solutions. *American Mineralogist* 81, 1425–1437. https://doi.org/10.2138/am-1996-11-1215

Holland, T.J.B., Powell, R. (2011) An improved and extended internally consistent thermodynamic dataset for phases of petrological interest, involving a new equation of state for solids. *Journal of Metamorphic Geology* 29, 333–383. https://doi.org/10.1111/j.1525-1314.2010.00923.x

Icenhower, J., London, D. (1995) An experimental study of element partitioning among biotite, muscovite, and coexisting peraluminous silicic melt at 200 MPa (H_2O). *American Mineralogist* 80, 1229–1251. https://doi.org/10.2138/am-1995-11-1213

Ji, M., Gao, X.-Y., Zheng, Y.-F., Meng, Z.-Y., Gao, P. (2021). Metapelites record two episodes of decompressional metamorphism in the Himalayan orogen. *Lithos* 394–395, 106183. https://doi.org/10.1016/j.lithos.2021.106183

Ji, M., Gao, X.-Y., Zheng, Y.-F. (2022) Geochemical evidence for partial melting of progressively varied crustal sources for leucogranites during the Oligocene–Miocene in the Himalayan orogen. *Chemical Geology* 589, 120674. https://doi.org/10.1016/j.chemgeo.2021.120674

Ji, M., Gao, X.-Y. Zheng, Y.-F. (2023) The petrogenetic relationship between migmatite and granite in the Himalayan orogen: Petrological and geochemical constraints. *Lithos* 444–445, 107110. https://doi.org/10.1016/j.lithos.2023.107110

Ji, M., Gao, X.-Y., Zheng, Y.-F. (2024a) Progressively elevated geothermal gradients for Miocene metamorphism in the Himalayan orogen. *Geological Society of America Bulletin* 136, 964–988. https://doi.org/10.1130/B36892

Ji, M., Gao, X.-Y., Xia, Q.-X., Zheng, Y.-F. (2024b) Secular change of metamorphic features in the Himalayan orogen during the Cenozoic and its tectonic implications. *Earth-Science Reviews* 248, 104640. https://doi.org/10.1016/j.earscirev.2023.104640

Knesel, K.M., Davidson, J.P. (2002) Insights into collisional magmatism from isotopic fingerprints of melting reactions. *Science* 296, 2206–2208. https://doi.org/10.1126/science.1070622

Kohn, M.J. (2014) Himalayan metamorphism and its tectonic implications. *Annual Review of Earth and Planetary Sciences* 42, 381–419. https://doi.org/10.1146/annurev-earth-060313-055005

Liu, Z.-C., Wu, F.-Y., Ding, L., Liu, X.-C., Wang, J.-G., Ji, W.-Q. (2016) Highly fractionated Late Eocene (~ 35 Ma) leucogranite in the Xiaru Dome, Tethyan Himalaya, South Tibet. *Lithos* 240, 337–354. https://doi.org/10.1016/j.lithos.2015.11.026

Nash, W.P., Crecraft, H.R. (1985) Partition coefficients for trace elements in silicic magmas. *Geochimica et Cosmochimica Acta* 49, 2309–2322. https://doi.org/10.1016/0016-7037(85)90231-5

Nesbitt, H., Young, G.M. (1982) Early Proterozoic climates and plate motions inferred from major element chemistry of lutites. *Nature* 299, 715–717. https://doi.org/10.1038/299715a0

Nier, A.O. (1938) The isotopic constitution of strontium, barium, bismuth, thallium and mercury. *Physical Review Journals Archive* 54, 175. https://doi.org/10.1103/PhysRev.54.275

Patiño Douce, A.E., Harris, N. (1998) Experimental constraints on Himalayan anatexis. *Journal of Petrology* 39, 689–710. https://doi.org/10.1093/petroj/39.4.689

Richards, A., Parrish, R., Harris, N., Argles, T., Zhang, L. (2006) Correlation of lithotectonic units across the eastern Himalaya, Bhutan. *Geology* 34, 341–344. https://doi.org/10.1130/G22169.1

Scaillet, B., Pichavant, M., Roux, J. (1995) Experimental Crystallization of Leucogranite Magmas. *Journal of Petrology* 36, 663–705. https://doi.org/10.1093/petrology/36.3.663

Schauble, E.A. (2004) Applying stable isotope fractionation theory to new systems. *Reviews in Mineralogy and Geochemistry* 55, 65–111. https://doi.org/10.2138/gsrmg.55.1.65

Shannon, R.D. (1976) Revised effective ionic radii and systematic studies of interatomic distances in halides and chalcogenides. *Acta Crystallographica Section A* 32, 751-767. https://doi.org/10.1107/S0567739476001551

Shaw, D.M. (1970) Trace element fractionation during anatexis. *Geochimica et Cosmochimica Acta* 34, 237–243. https://doi.org/10.1016/0016-7037(70)90009-8

Sun, C., Craff, M., Liang, Y. (2017) Trace element partitioning between plagioclase and silicate melt: the importance of temperature and plagioclase composition, with implications for terrestrial and lunar magmatism. *Geochimica et Cosmochimica Acta* 206, 273–295. https://doi.org/10.1016/j.gca.2017.03.003

Urey, H.C. (1947) The thermodynamic properties of isotopic substances. *Journal of the Chemical Society* 562–581. https://doi.org/10.1039/jr9470000562

Wang, J., Wu, F., Zhang, J., Khanal, G., Yang, L. (2022) The Himalayan Collisional Orogeny: A Metamorphic Perspective. *Acta Geologica Sinica (English Edition)* 96, 1842–1866. https://doi.org/10.1111/1755-6724.15022

Weinberg, R.F. (2016) Himalayan leucogranites and migmatites: nature, timing and duration of anatexis. *Journal of Metamorphic Geology* 34, 821–843. https://doi.org/10.1111/jmg.12204

White, R.W., Powell, R., Holland, T.J.B., Worley, B.A. (2000) The effect of TiO_2 and Fe_2O_3 on metapelitic assemblages at greenschist and amphibolite facies conditions: mineral equilibria calculations in the system K_2O–FeO–MgO–Al_2O_3–SiO_2–H_2O–TiO_2–Fe_2O_3. *Journal of Metamorphic Geology* 18, 497–511. https://doi.org/10.1046/j.1525-1314.2000.00269.x

White, R.W., Powell, R., Clarke, G.L. (2002) The interpretation of reaction textures in Fe-rich metapelitic granulites of the Musgrave Block, central Australia: constraints from mineral equilibria calculations in the system K_2O–FeO–MgO–Al_2O_3–SiO_2–H_2O–TiO_2–Fe_2O_3. *Journal of Metamorphic Geology* 20, 41–55. https://doi.org/10.1046/j.0263-4929.2001.00349.x

White, R.W., Powell, R., Holland, T.J.B., Johnson, T.E., Green, E.C.R. (2014) New mineral activity–composition relations for thermodynamic calculations in metapelitic systems. *Journal of Metamorphic Geology* 32, 261–286. https://doi.org/10.1111/jmg.12071

Whitney, D.L., Evans, B.W. (2010) Abbreviations for names of rock-forming minerals. *American Mineralogist* 95, 185–187. https://doi.org/10.2138/am.2010.3371

Wood, B.J., Blundy, J.D. (1997) A predictive model for rare earth element partitioning between clinpyroxene and anhydrous silicate melt. *Contributions of Mineralogy and Petrology* 129, 166–181. https://doi.org/10.1007/s004100050330

Wu, F.-Y., Liu, X.-C., Liu, Z.-C., Wang, R.-C., Xie, L., Wang, J.-M., Ji, W.-Q., Yang, L., Liu, C., Khanal, G.P., HE, S.-X. (2020) Highly fractionated Himalayan leucogranites and associated rare-metal mineralization. *Lithos* 352–353, 105319. https://doi.org/10.1016/j.lithos.2019.105319

Xu, Z.-Q., Wang, Q., Pecher, A., Liang, F., Qi, X.-X., Cai, Z.-H., Li, H.-Q., Zeng, L.-S., Cao, H. (2013) Orogen-parallel ductile extension and extrusion of the Greater Himalaya in the late Oligocene and Miocene. *Tectonics* 32, 191–215. https://doi.org/10.1002/tect.20021

Yin, A. (2006) Cenozoic tectonic evolution of the Himalayan orogen as constrained by along-strike variation of structural geometry, exhumation history, and foreland sedimentation. *Earth-Science Reviews* 76, 1–131. https://doi.org/1005-2321(2006)13:5<416:XMLYZS>2.0.TX;2-X

Yin, A., Harrison, T.M. (2000) Geologic evolution of the Himalayan-Tibetan orogen. *Annual Review of Earth and Planetary Sciences* 28, 211–280. https://doi.org/10.1146/annurev.earth.28.1.211

Zeng, L.S., Gao, L.E., Xie, K.J., Liu-Zeng, J. (2011) Mid-Eocene high Sr/Y granites in the Northern Himalayan Gneiss Domes: melting thickened lower continental crust. *Earth and Planetary Science Letters* 303, 251–266. https://doi.org/10.1016/j.epsl.2011.01.005

Zhang, Y, Yang, J.-H., Chen, J.-Y, Wang, H., Xiang, Y.-X. (2017) Petrogenesis of Jurassic tungsten-bearing granites in the Nanling Range, South China: Evidence from whole-rock geochemistry and zircon U-Pb and Hf-O isotopes. *Lithos* 278–281, 166–180. http://doi: 10.1016/j.lithos.2017.01.018